Supplement of Biogeosciences, 23, 8159–8181, 2026
https://doi.org/10.5194/bg-23-8159-2026-supplement
© Author(s) 2026. CC BY 4.0 License.



Biogeosciences Open Access EGU

Supplement of

Assessment of vegetation water dynamics by comparing microwave remote sensing signals from satellites and field-based GNSS reflectometry

Andrew F. Feldman et al.

Correspondence to: Andrew F. Feldman (afeld24@umd.edu)

The copyright of individual parts of the supplement might differ from the article licence.

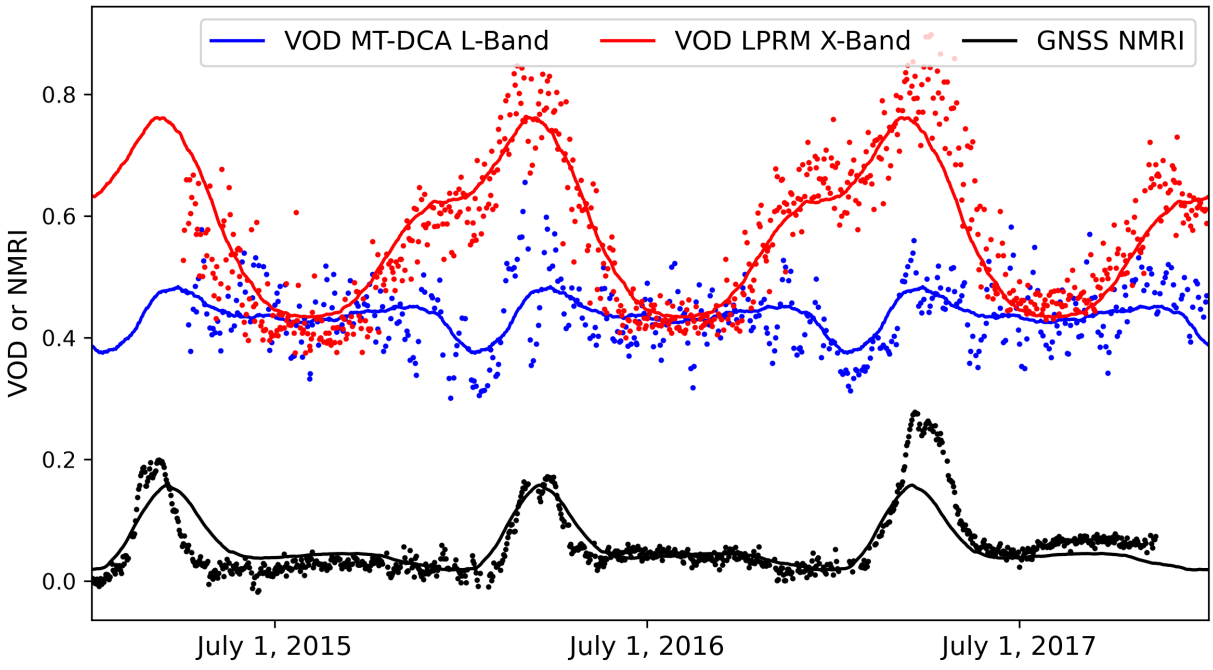


Figure S1. Example representative site at 36.12°N and 120.44°W (same as Fig. S2 at the p294 PBO site) showing time series of L-band and X-band VOD as well as GNSS-IR NMRI. The solid lines are an average climatology built based on averaging data over the three years and smoothing them with a moving window. Seasonal timing analyses are based on the averaged smoothed climatologies.

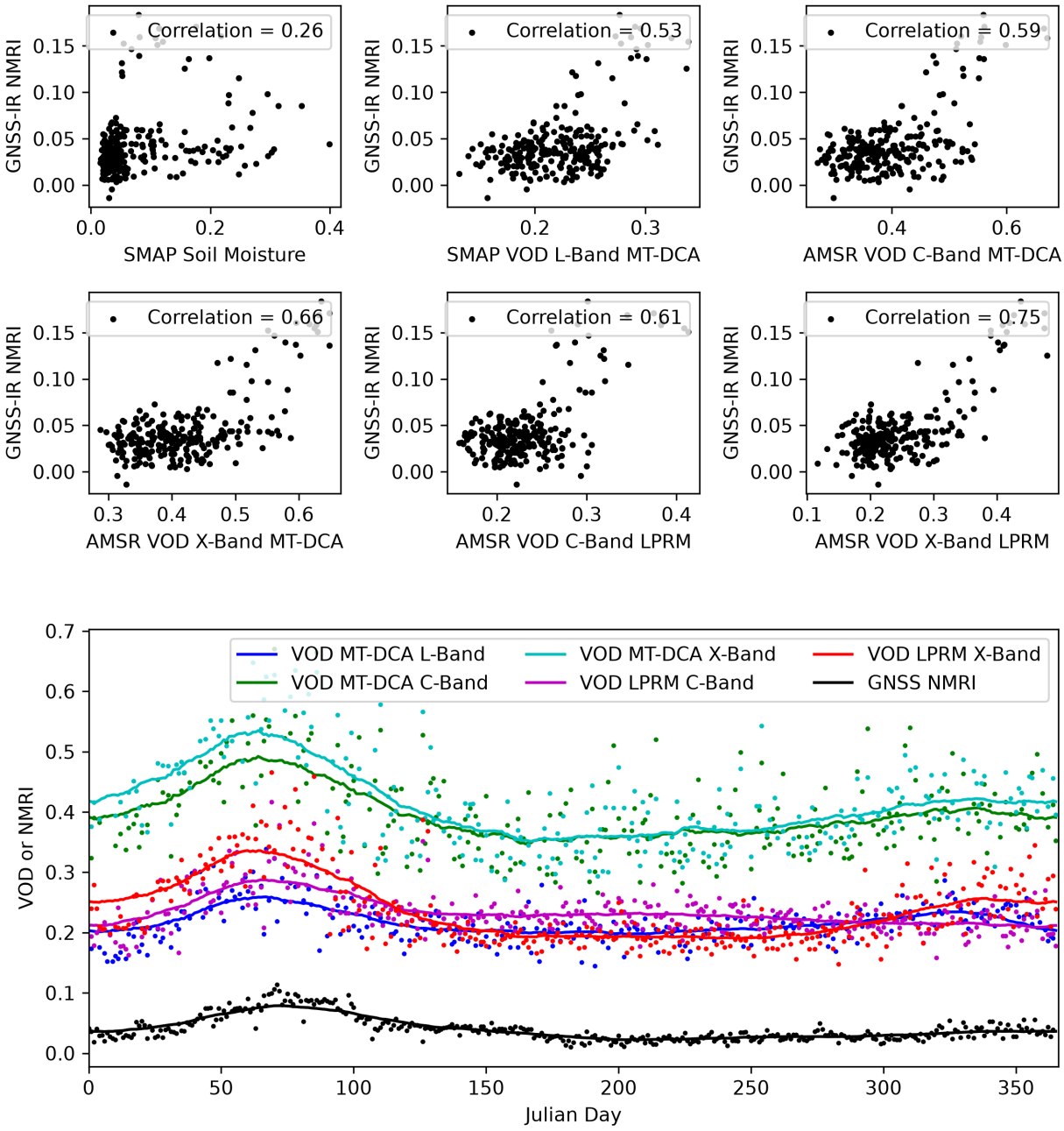


Figure S2. Example site at 36.12°N and 120.44°W (same as Fig. S1 at the p294 PBO site) with demonstrated relationships and correlations between GNSS-IR and soil moisture and VOD metrics on Figure 1. Time series of the three-year averaged VOD and NMRI (2015-2017) in dots symbols as well as smoothed climatology as solid lines.

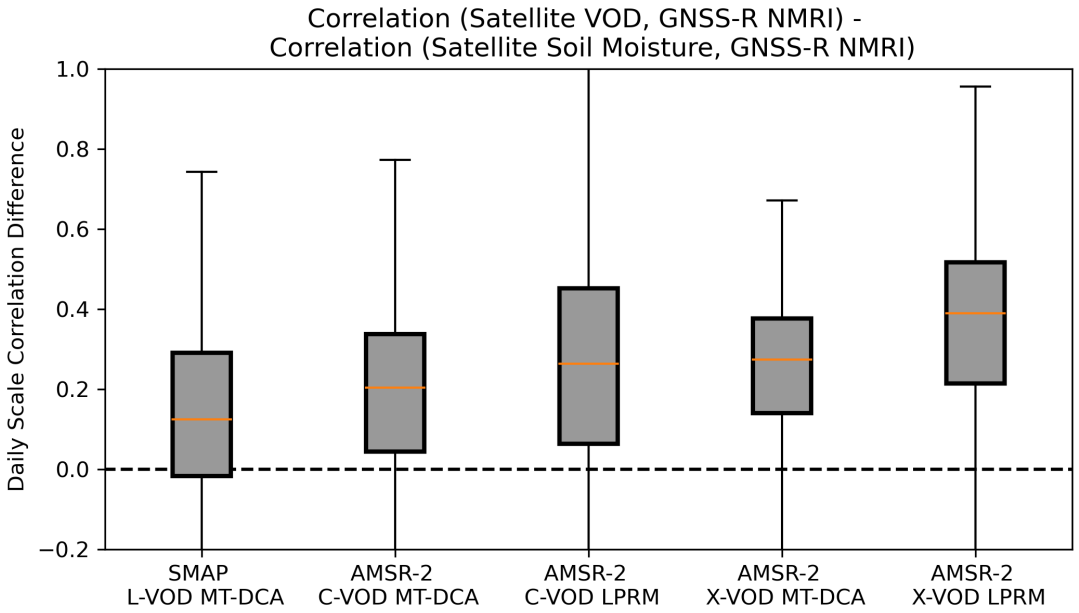


Figure S3. Difference of correlations between VOD metrics with GNSS NMRI and correlations between SMAP soil moisture with GNSS NMRI. Positive values indicate higher positive correlations between VOD with GNSS NMRI than soil moisture with GNSS NMRI.

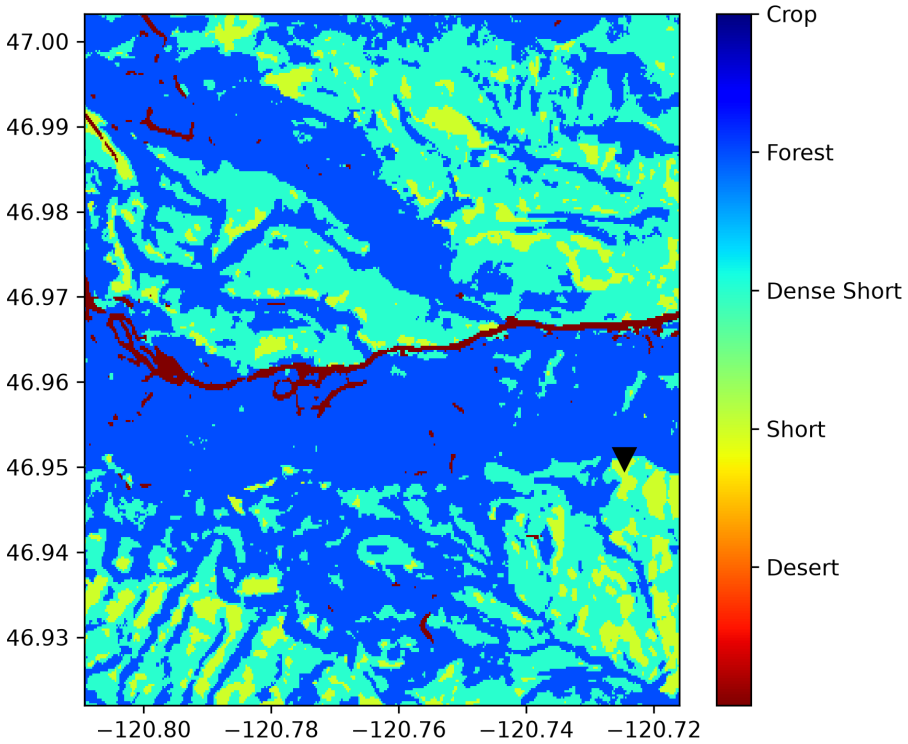


Figure S4. Example PBO H2O GNSS-IR site (at the sc00 PBO site) at 46.95°N, 120.72°W as marked by a black triangle symbol. The background color is the land cover over the associated 9km SMAP pixel. This site contains short-statured vegetation, whereas forests dominate the 9km pixel. Therefore, the GNSS-IR site might mostly observe grass and/or shrub species, while the satellite radiometers might receive most of their signal from trees throughout the pixel.

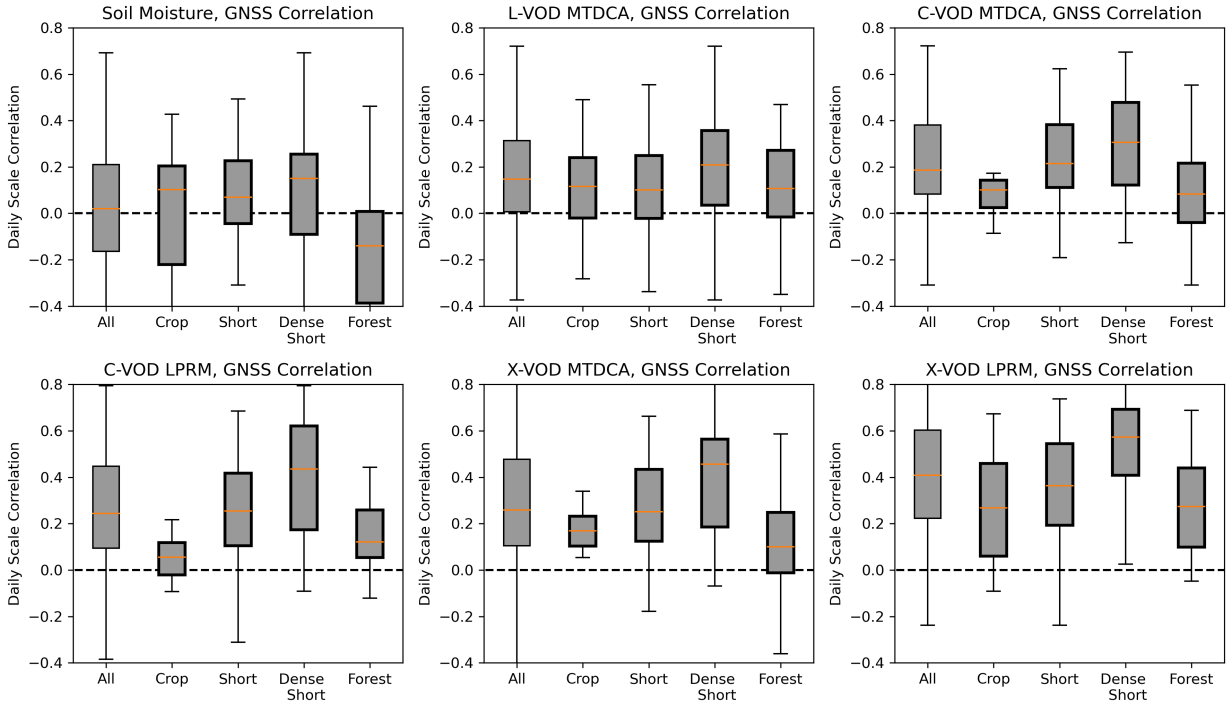


Figure S5. Same as Figure 3 but considering the dominant land cover for the 9km satellite pixel instead of at a given site.

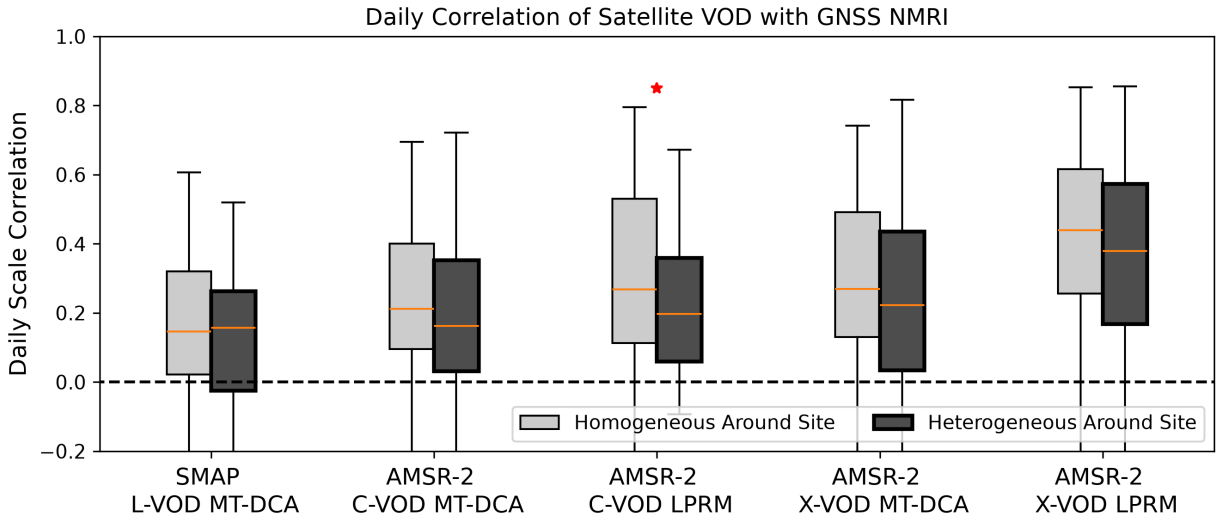


Figure S6. Same as Figure 4a, but considering cases where the land cover classifications in the 90m x 90m area around each site (3x3 grid of 30m x 30m pixels) are the same (homogeneous) or varying (heterogeneous).

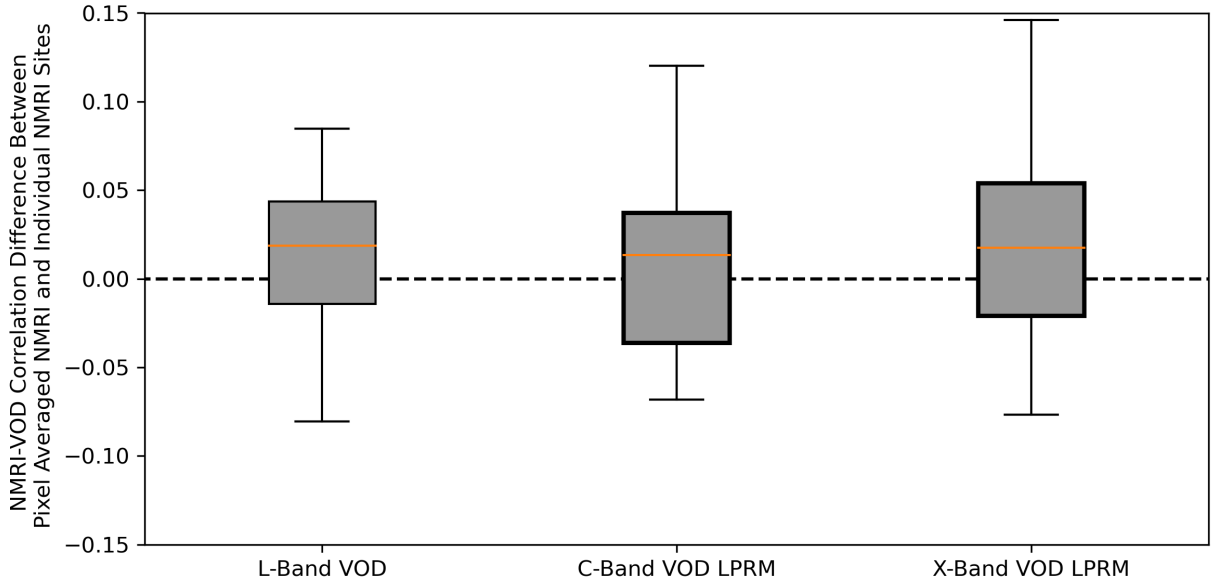


Figure S7. For the six pixels that contain multiple GNSS-IR sites, correlation differences between averaging the NMRI time series across the sites and individual NMRI time series. For this analysis, we only evaluated the VOD data products with 9km gridding.

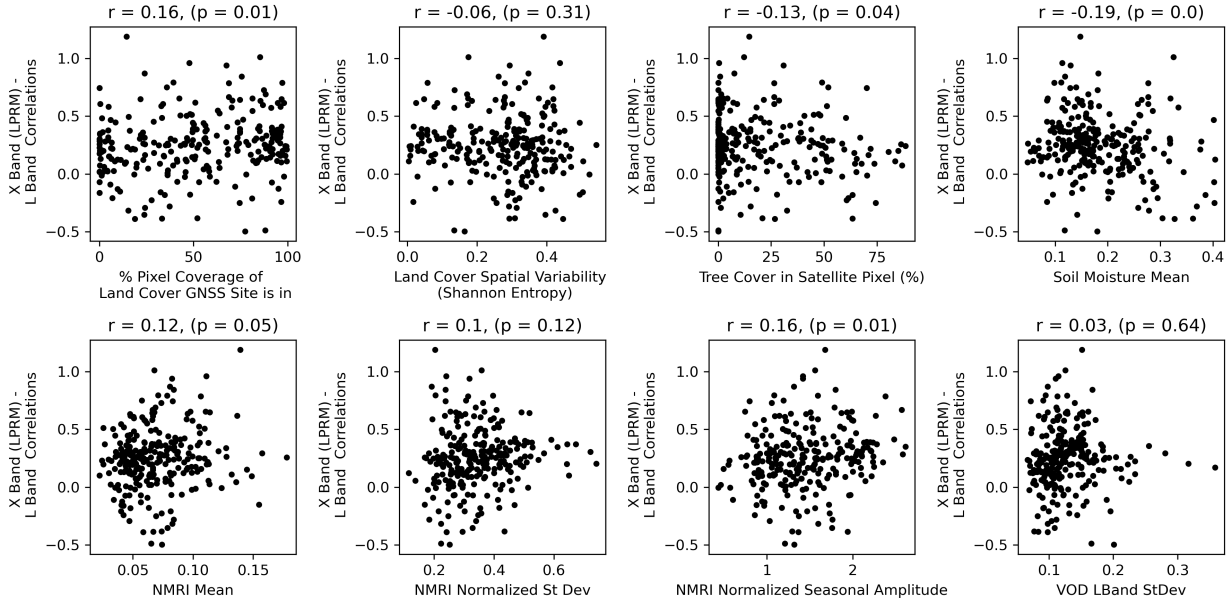


Figure S8. The potential drivers of the difference between the NMRI correlations with X-band VOD from LPRM and L-band VOD MT-DCA algorithms. These relationships are shown in bar plots in Figs. 5c and 5d.

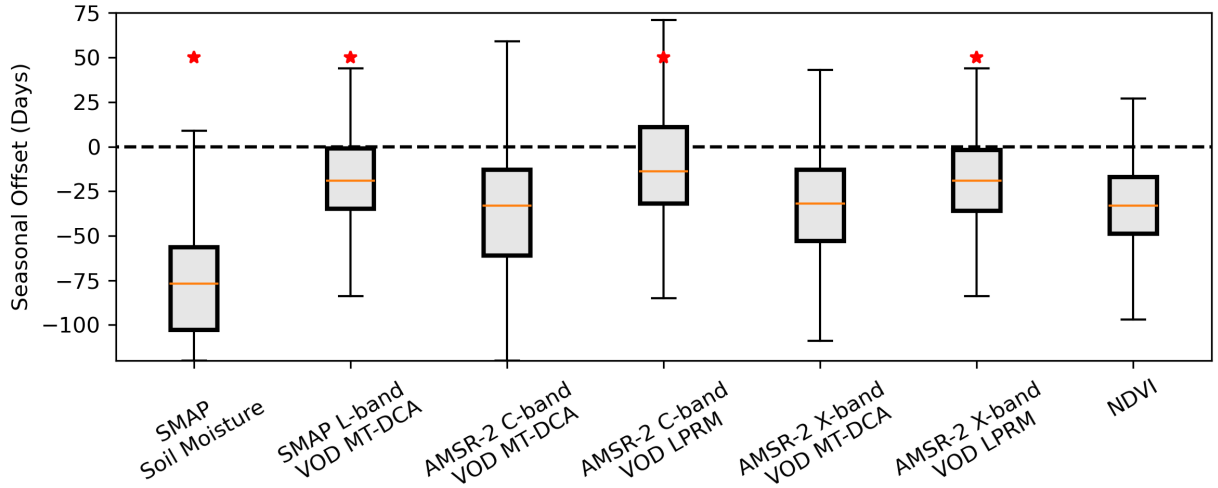


Figure S9. Same as Fig. 7, but using maximum cross correlation timing to estimate the seasonal offset between the respective metric and NMRI. Symbols represent that variable having a statistically significantly (p<0.05) different offset with NMRI than NDVI and NMRI.

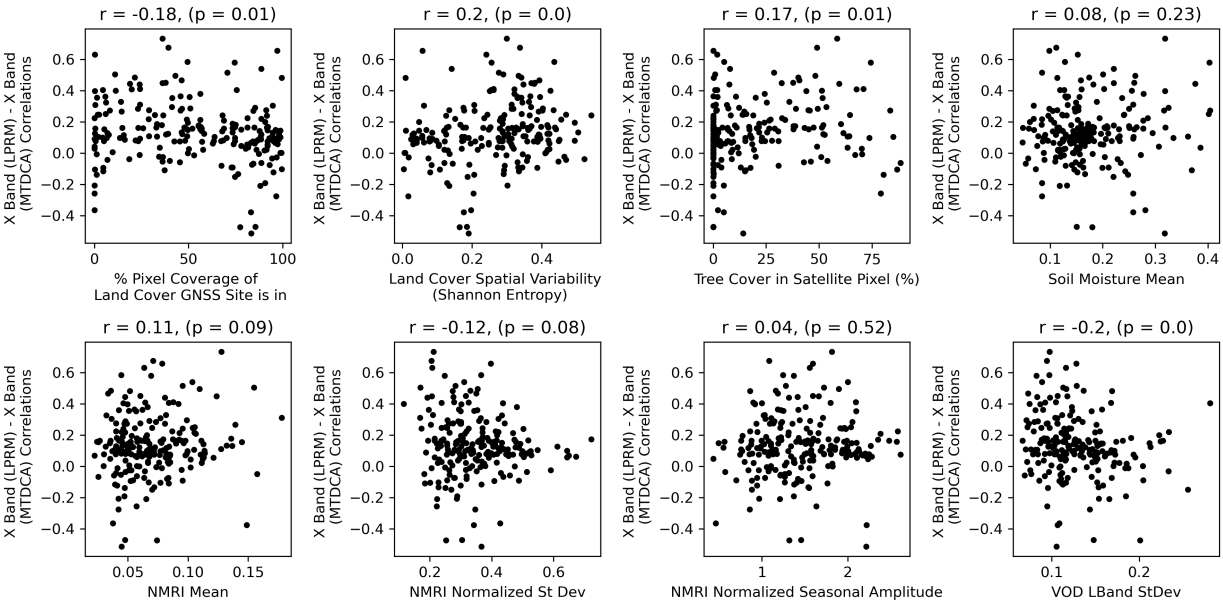


Figure S10. The potential drivers of the difference between the NMRI correlations with X-band VOD from LPRM and MT-DCA algorithms corresponding to Fig. 9.

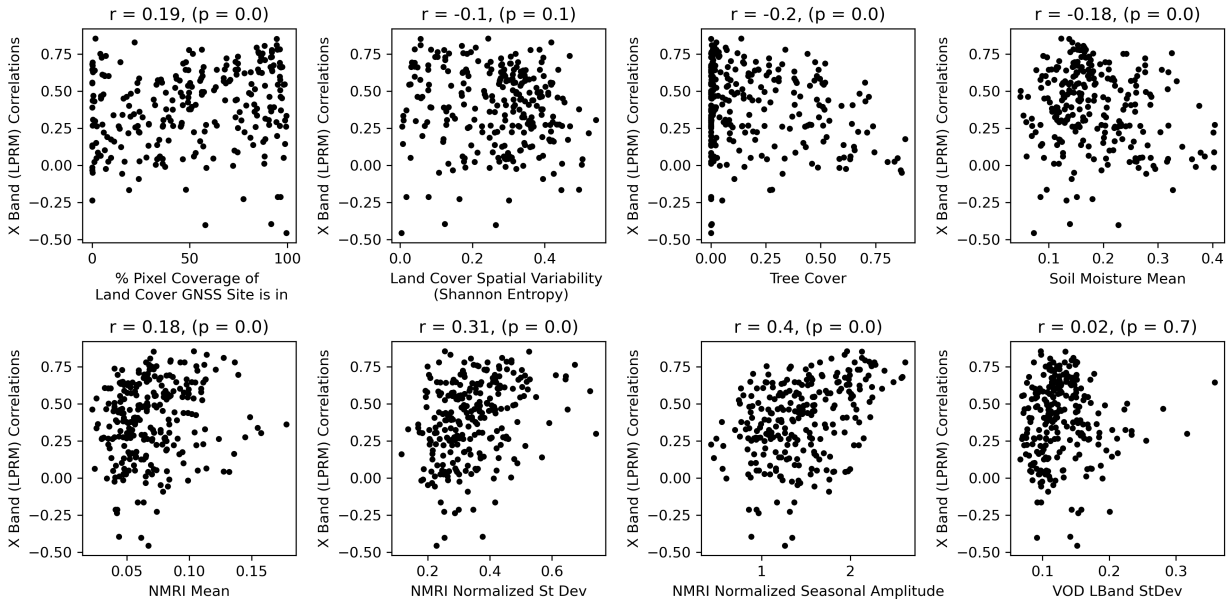


Figure S11. Individual explanatory variables used in Fig. 10 regressed individually on X-band LPRM correlations with NMRI as an example.

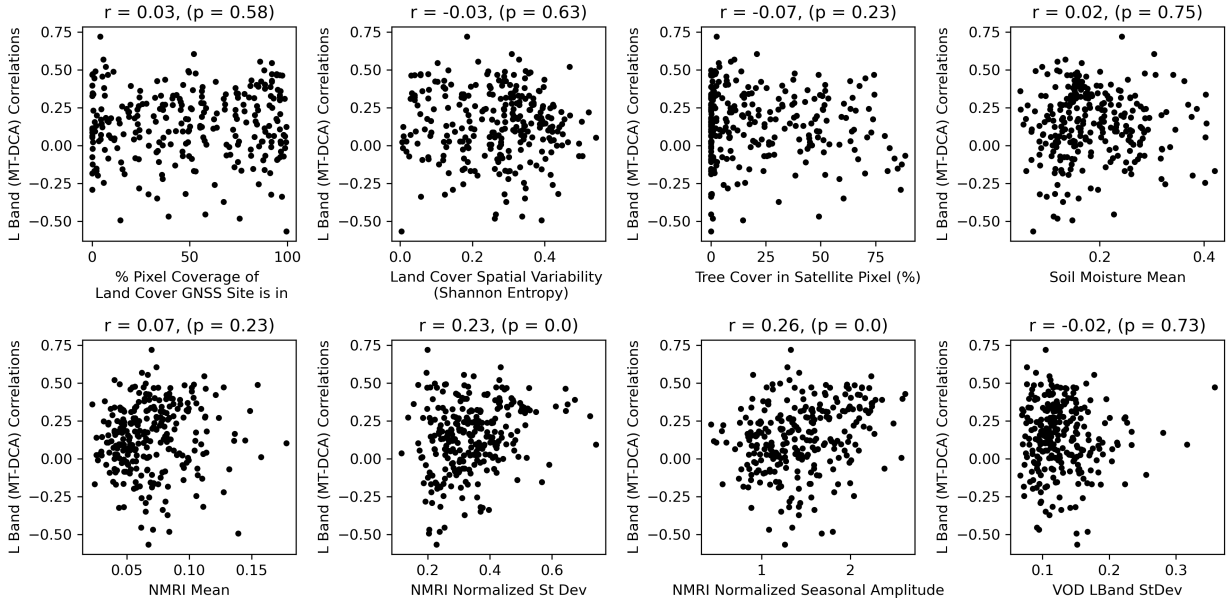


Figure S12. Same as Fig. S11, but for L-band MT-DCA VOD.

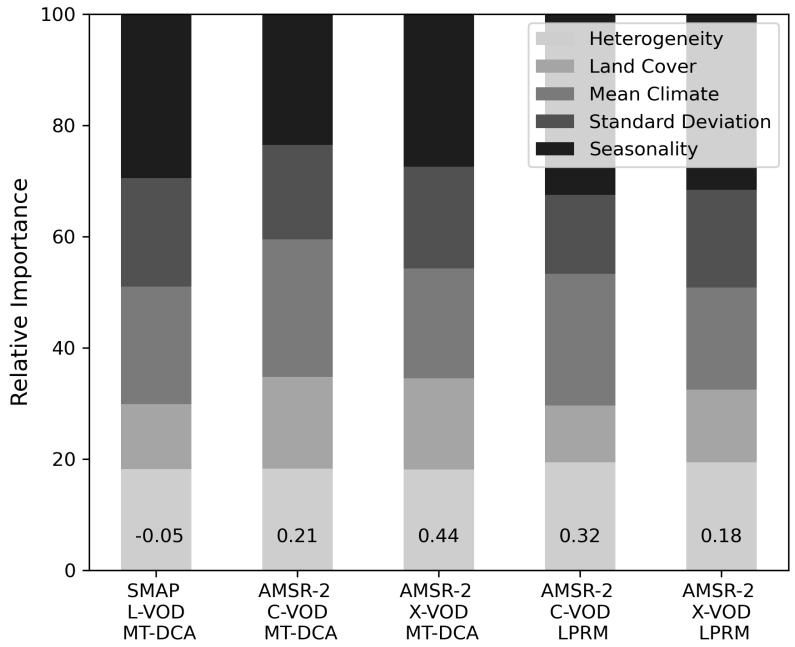


Figure S13. Same as Figure 10a, but repeating using the random forest regression approach.